Numerical investigation of the three-dimensional dynamic process of sabot discard[†]

HUANG Zhen-gui, WESSAM Mahfouz Elnaggar and CHEN Zhi-hua[*]

Key Laboratory of Transient Physics, Nanjing University of Science and Technology, Nanjing 210094, Jiangsu, China

---

Abstract

The sabot discard process of an armor-piercing, fin-stabilized discarding sabot (APFSDS) is crucial for the flight stability of the projectile. In this paper, the sabot discard behavior after projectile ejection from the muzzle is investigated at Mach number 4.0 and angle of attack of 0°. 3D compressible equations implemented with a dynamic unstructured tetrahedral mesh are numerically solved with a commercial computational fluid dynamics (CFD) code (FLUENT 12.0). Six-degrees-of-freedom (6DOF) rigid-body motion equations is solved with the CFD results through a user-defined function to update the sabot trajectory at every time step. A combination of spring-based smoothing and local re-meshing is employed to regenerate the meshes around the sabot and describe its movement at each time step. Computational results show three different separation processes during the sabot discard process. Furthermore, the aerodynamic forces of APFSDS are calculated, and the trajectories of the three sabots are illustrated through the numerical solution of 6DOF equations. The results of the present study agree well with typical experimental results and provide detailed parameters that are important for analyzing the stability of the projectile. The present computations confirm that the numerical solution of the governing equations of aerodynamics and 6DOF rigid-body equations are a feasible method to study the sabot discard processes of APFSDS.

Keywords: APFSDS; Dynamic mesh; Sabot discard; Six degrees of freedom; User-defined function

---

1. Introduction

With the rapid development of high-performance computing and numerical algorithms, computational fluid dynamics (CFD) has become a highly effective alternative to acquire more accurate solutions for complex flow field problems associated with projectile and missile systems [1-3]. The focus of this study is to utilize CFD technologies in investigating the dynamic sabot discard process of an armor-piercing, fin-stabilized discarding sabot (APFSDS). The sabot is a device usually made up of two or more petals that encase the projectile and provide it with required structural support to withstand high-acceleration loads during launch [4]. The sabot is also utilized to fill the space between the barrel wall and the projectile to prevent muzzle gases from blowing by the projectile [5]; therefore, as a sub-caliber projectile, APFSDS can be fired from a smooth bore gun.

After launch, the sabot becomes a parasitic mass and must be discarded as quickly as possible to allow the projectile to fly in a free and low-drag condition. This action is normally accomplished by incorporating a scoop into the front of the sabot so that aerodynamic forces can strip each sabot from the projectile. Thus, understanding the dynamical process of sabot discard, including detailed sabot aerodynamics, is essential to ensure that the sabot separates quickly without inducing other perturbing forces that could adversely affect the trajectory of the penetrator.

Investigations have shown that although numerous interferences may result in the alteration of the projectile trajectory during the process of sabot discard, aerodynamic interference is the main source of launch disturbance and can lead to an unacceptable loss of accuracy [6, 7]. Many researchers have analyzed several critical aspects, and some advancement has been achieved over the past few decades. Investigations were traditionally accomplished with shooting tests and engineering analytical studies [6-8]. However, these methods are time consuming; normally, much time is required to acquire accurate data. In addition, such types of experiments often pose danger to the experimenters and apparatus because of the unexpected motion of the sabot and projectile during tests. Increased efforts have been carried out to study the aerodynamics of sabot discard; for example, the mutual interference of the flows among the projectile and three sabot petals with splitter plates was examined through wind-tunnel tests at Mach number 4.5 [5]. The experimental results revealed the regions of shock/shock interaction and the collision of shock and sabot/projectile. Moreover, a series of wind-tunnel experiments on more sophisticated sabot petals were performed to obtain the surface pressure of the front scoop and interior of

*Corresponding author. Tel.: +86 2584303929, Fax.: +86 25 84315644
E-mail address: chenzh@mail.njust.edu.cn
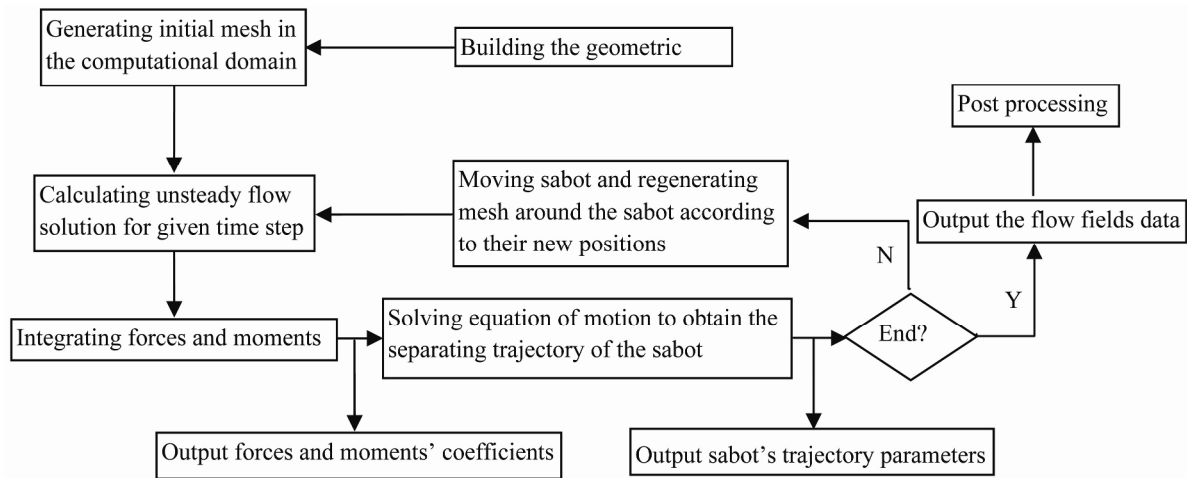[†] Recommended by Associate Editor Do Hyung Lee

Fig. 1. Unsteady simulation procedures.

sabots at different stages of the discard process [9, 10]. The static pressure on the front scoop and interior was measured and utilized as reference in the sabot design. Nevertheless, wind tunnel tests are expensive, and loss of accuracy occurs in certain situations. The disadvantage of shooting and wind tunnel tests is that real-time measurement of the aerodynamic forces and moments, positions, and attitudes of the sabot and projectile as well as the involved flow properties cannot be implemented.

Meanwhile, the complex flow fields and the dynamic discard process of sabots can be described and illustrated based on CFD results. The steady axisymmetric flow fields of APFSDS with different fixed positions of the discard sabot were simulated based on multi-block mesh generation technology [11, 12]. The flow structure and surface pressure distribution of the sabot and projectile were calculated to describe the discard process. Multi-rigid body movement, with the introduction of Chimera overset grid approaches [13-15] and dynamic unstructured tetrahedral mesh approaches [16, 17], has also been applied in simulations. Based on 2D Euler equations, three different shapes of the sabot during discard processes have been simulated under intermediate ballistic flow conditions [18]. The results were validated through an experimental test. Based on Euler equations and two immiscible gases with fixed Cartesian meshes, detailed firing experiments have also been conducted with a 120 mm APFSDS projectile [19, 20]. The simulated pressure results agreed well with the corresponding firing experimental results. Numerical investigations have also been performed for a sabot located at different positions with respect to the projectile [21, 22] and different sabot shapes [4, 23].

However, only a few numerical results exist concerning the coupling between the 3D unsteady aerodynamics and six-degrees-of-freedom (6DOF) rigid-body motion of a sabot. This study aims to thoroughly investigate the sabot discard process after projectile ejection from the gun barrel. A 6DOF model coupled with the FLUENT solver through a user-defined function (UDF) and dynamic unstructured tetrahedral mesh technology was applied to simulate the sabot discard process at Mach number 4.0 and angle of attack of 0°. The flow fields and discard trajectories of the sabot during the discard process were obtained and discussed.

2. Numerical methods and physical model

The numerical solutions in this study were obtained with FLUENT and 6DOF solvers. A flow solver was utilized to solve the aerodynamic governing equations. The aerodynamic forces and moments acting on the sabot were computed by integrating pressure over the surface at each time step. Additional load forces (e.g., injecting forces, thrust, gravitational force) and moments can also be added to the 6DOF equations. The position and attitude of the sabot can be obtained by the numerical simulation 6DOF equations. Fig. 1 shows the numerical simulation procedures.

2.1 Flow solver

The governing equations for compressible flow are continuity, momentum, and energy equations. The conservation of mass equation (continuity equation) can be written as follows:

$$\frac{\partial \rho}{\partial t} + \nabla \bullet (\rho \vec{v}) = 0 . \tag{1}$$

The conservation of momentum equation is

$$\frac{\partial}{\partial t}(\rho \vec{v}) + \nabla \bullet (\rho \vec{v} \vec{v}) = -\nabla p + \rho \vec{g} + \vec{F} \tag{2}$$

where p is the static pressure, $\rho \vec{g}$ is the gravitational body force vector, and $\vec{F}$ is the external body force vector.

The conservation of energy equation is

$$\frac{\partial E}{\partial t} + \nabla \bullet \left(\vec{v}\left(E + p \right) \right) = 0 \tag{3}$$

where E is the total energy per mass.

$$E = \frac{p}{(\gamma - 1)\rho} + \frac{1}{2}\left(v_x^2 + v_y^2 + v_z^2 \right) \tag{4}$$

$\gamma = 1.4$ is the specific heat ratio.

The ideal gas equation of state is defined as

$$p = \rho R T \tag{5}$$

where R is the gas constant.

Eqs. (1)-(5) constitute the closed system of governing equations. FLUENT employs a cell-centered finite volume method to solve these equations in integral form. The cell-centered finite volume is based on the linear reconstruction scheme, which allows the use of computational elements with arbitrary polyhedral topology. A point-implicit (block Gauss-Seidel) linear equation solver is utilized in conjunction with an algebraic multi-grid method to solve all dependent variables in each cell. A second-order implicit AUSM scheme is employed for the convection term. The detailed formulations and methods are available in Ref. [24].

With respect to dynamic meshes, the integral form of the conservation equation for a general scalar, on an arbitrary control volume, V, whose boundary is moving, can be written as

$$\frac{d}{dt}\int_V \rho\phi dV + \int_{\partial V} \rho\phi\left(\vec{u} - \vec{u}_g\right)\bullet d\vec{A} = \int_{\partial V} \Gamma\,\nabla\phi\bullet d\vec{A} + \int_V S_\phi dV \tag{6}$$

where $\vec{u}$ is the flow velocity vector, $\vec{u}_g$ is the mesh velocity vector of the moving mesh, Γ is the diffusion coefficient, and S_ϕ is the source term of ϕ. $\vec{A}$ and ∂V are utilized to represent the surface area vector and boundary of the control volume, respectively.

$$\frac{d}{dt}\int_V \rho\phi dV = \frac{\left(\rho\phi V\right)^{n+1} - \left(\rho\phi V\right)^n}{\Delta t} \tag{7}$$

where the indices n and $n+1$ denote the quantity at the current and next time level, respectively. The $(n+1)^{\text{th}}$ time level volume, V^{n+1}, is evaluated as

$$V^{n+1} = V^n + \frac{dV}{dt}\Delta t \tag{8}$$

where dV/dt is the volume-time derivative of the control volume. To satisfy the mesh conservation law, the volume-time derivative of the control volume is evaluated as

$$\frac{dV}{dt} = \int_{\partial V} \vec{u}_g \cdot d\vec{A} = \sum_j^{n_f} \vec{u}_{g,j} \cdot \vec{A}_j \tag{9}$$

where n_f is the number of faces on the control volume and $\vec{A}_j$ is the j face surface area vector.

The dot product $\vec{u}_{g,j} \bullet \vec{A}_j$ on each control volume face is calculated as

$$\vec{u}_{g,j} \bullet \vec{A}_j = \frac{\delta V_j}{\Delta t} \tag{10}$$

where δV_j is the volume swept out by control volume face j over the time step Δt.

The gradient of ϕ in Eq. (6) was utilized to discretize the convection and diffusion terms, which were computed with the node-based method of Green-Gauss in the flow conservation equations. The node-based gradient is known to be more accurate than the cell-based gradient, particularly on irregular (skewed and distorted), unstructured meshes.

2.2 6DOF model for trajectory calculation

The flight of the sabot and projectile were described with 6DOF motion equations, which can be calculated by coupling with Euler equations using UDF in FLUENT. UDF is a function written by the user that is dynamically linked with the FLUENT solver at run time. The 6DOF solver employs forces and moments calculated by the integration of pressure over the body surface.

The 6DOF motion is represented by the translational position of the center of gravity (CG) and the rotation of the sabot. The governing equation (Newton's equation) for the translational motion is solved in the inertial coordinate system as follows:

$$\dot{\vec{v}}_G = \frac{1}{m}\sum \vec{f}_G \tag{11}$$

where $\dot{\vec{v}}_G$ is the translational motion of the center of gravity, m is the mass of the sabot, and $\vec{f}_G$ is the force vector that includes three components: aerodynamic forces, external applied forces (such as thrust), and forces caused by gravity. Eq. (11) can be calculated directly with the given translation acceleration of CG.

Angular motion is governed by Euler's equations of motion and can be easily computed using body coordinates to avoid time-variant inertia properties. The body axes are specified to coincide with the principal axes of inertia of the coordinate system. Euler's equation is then written as

$$\dot{\vec{\omega}}_B = \boldsymbol{L}^{-1}\left(\sum \vec{M}_B - \vec{\omega}_B \times \boldsymbol{L}\vec{\omega}_B\right) \tag{12}$$

where subscript $_B$ means that the variable is calculated in the body coordinates, $\boldsymbol{L}$ is the inertia tensor, $\vec{M}_B$ is the moment vector of the body, and $\vec{\omega}_B$ is the rigid body angular velocity vector.

The orientation of the sabot is tracked using a standard 3-2-

1 Euler rotation sequence. The moments are therefore transformed from inertial to body coordinates via

$$\vec{M}_B = \mathbf{R}\vec{M}_G \tag{13}$$

where $\mathbf{R}$ represents the following transformation matrix from inertial to body coordinates:

$$\mathbf{R} \equiv \begin{bmatrix} C_\theta C_\psi & C_\theta S_\psi & -S_\theta \\ S_\phi S_\theta C_\psi - C_\phi S_\psi & S_\phi S_\theta S_\psi & S_\phi C_\theta \\ C_\phi S_\theta C_\psi + S_\phi S_\psi & C_\phi S_\theta S_\psi - S_\phi C_\psi & C_\phi C_\theta \end{bmatrix} \tag{14}$$

where the shorthand notation $C_\chi = \cos(\chi)$ and $S_\chi = \sin(\chi)$ were used. ϕ, θ, and ψ are the Euler angles that represent rotation on x-axis, y-axis, and z-axis, respectively.

Once the translational and angular accelerations are computed from Eqs. (11) and (12), the angular and translational velocities are determined using a fourth-order multi-point Adams-Moulton formulation.

$$\xi^{k+1} = \xi^k + \frac{\Delta}{24}\left(9\dot{\xi}^{k+1} + 19\dot{\xi}^k - 5\dot{\xi}^{k-1} + \dot{\xi}^{k-2}\right) \tag{15}$$

where ξ represents either $\vec{v}_G$ or $\vec{\omega}_B$.

The dynamic mesh algorithm employs $\vec{v}_G$ and $\vec{\omega}_G$ as input to update the rigid body position. Angular velocity must then be transformed back to inertial coordinates via

$$\vec{M}_G = \mathbf{R}^T \vec{M}_B \tag{16}$$

where $\mathbf{R}$ is given in Eq. (14).

The locations and attitudes of the rigid body are obtained by solving the kinematical equations on the foundation of the previously computed $\vec{v}_G$ and $\vec{\omega}_G$. The kinematical equations are well known and are thus not shown for the sake of brevity.

2.3 Dynamic mesh

An unstructured dynamic mesh approach consisting of spring-based smoothing and local re-meshing was developed to accommodate the moving sabot in the discretized computational domain. Given the movement of the sabot, the mesh was stretched; therefore, the nodes must be moved to improve the grid quality. The so-called spring-based smoothing method was adopted to determine the new nodal location. The cell edges between mesh nodes were idealized as a network of interconnected springs. The movement of the boundary node was propagated into the volume mesh because of the spring force generated by the elongation or contraction of the edges connected to the node. At equilibrium, the sum of the spring forces at each node must be zero.

After the movement of the boundary nodes based on the calculated results of 6DOF equations, the new nodes must be
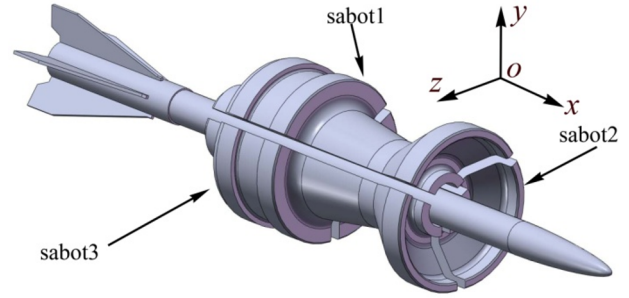

Fig. 2. APFSDS geometric model.

updated to regain equilibrium. When the motion of the sabot is large compared with the local cell size, the mesh quality is no longer sufficiently maintained through the spring-based smoothing method. This condition will invalidate the mesh (for example, result in negative cell volumes) and consequently lead to convergence problems when the solution is updated in the next time step. Therefore, poor-quality cells (based on volume or skewness criteria) agglomerate and must be remeshed with the solution interpolated from the old cells through the local re-meshing method.

2.4 Physical model and computational mesh

Fig. 2 shows the APFSDS geometry configuration and the global coordinate system. The centerline of the projectile lies along the x axis with the positive direction toward the projectile tip. The y axis points upward along the negative direction of the gravity, and the z axis is determined by the right hand rule. The origin of the coordinate system is located at the center of the rear circle surface of the projectile. The geometry configuration consists of a 522 mm long projectile, which is made of tungsten and consists of three sabot petals and five fins. Therefore, the projectile is regarded as a rigid body.

The projectile is assumed to have zero yaw and pitch angles and has a length-to-diameter ratio (L/D) of 23.73. Its total mass is 5.6 kg, including a sabot mass of approximately 0.573 kg. The reference area and length utilized to calculate aerodynamic coefficients are 380.13 mm^2 and 522 mm, respectively. Three sabot petals characterized by aerodynamic force separation are parallel to the projectile, with a gap of approximately 4 mm at the initial time. For this type of sabot configuration, the gap could be explained by the relaxation of the internal ballistic constraints of the sabot petals. In general, the sabot petals are facing away from the projectile with a relatively low velocity to the projectile at the time when the projectile is being ejected from the gun barrel. The initial velocities that cause the sabots to dissociate from the projectile are provided in Table 1. Other information, including the main geometrical data and several important initial conditions for calculating the discard trajectory and aerodynamic coefficients, are also shown in this table.

Table 1. Main geometrical data and initial conditions for sabot discard.

		Sabot 1	Sabot 2	Sabot 3
Initial CG from origin (m)	x	0.0	0.0	0.0
	y	0.028517024	-0.014258512	-0.014258512
	z	0.0	-0.024696467	0.024696467
Initial velocity (m/s)	v_x	0.0	0.0	0.0
	v_y	20	-10	-10
	v_z	0.0	-17.32	17.32
Initial Euler angle (degree)	x	0	-120	120
Initial Euler angle (degree)	y	0	0	0
Initial Euler angle (degree)	z	0	0	0
Moment of inertia (kg·m^2)	I_{xx}	0.0002277992	0.0002277992	0.0002277992
	I_{yy}	0.0018976127	0.0018165789	0.0018165789
	I_{zz}	0.0017895676	0.0018868501	0.0018706014
Product of inertia (kg·m^2)	I_{xy}	1.7348635e-5	-8.6743174e-6	-8.6743174e-6
	I_{xz}	0.0	-1.5024359e-5	-1.5024359e-5
	I_{yz}	0.0	-4.6784907e-5	4.6784907e-5
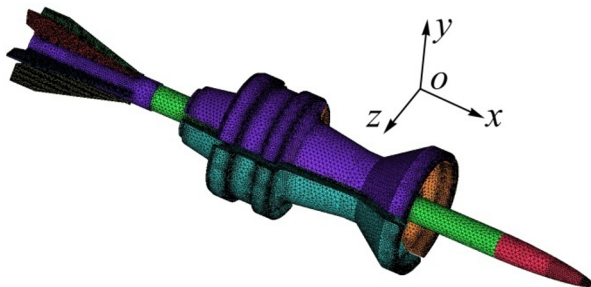
(a) Surface mesh of the projectile/sabot

(b) Detailed surface mesh of one sabot petal

Fig. 3. Surface mesh of the projectile and sabot.

A starting volume mesh must be provided to use the dynamic mesh. Based on previous results [25], APFSDS was simplified to generate better volume mesh and subsequently improve the precision of the solution. Fig. 3 shows the projectile/sabot surface mesh and the detailed surface mesh of one sabot petal for this numerical simulation. The number of tetrahedral mesh is approximately 8 million. These unstructured tetrahedral meshes were built with ICEM-CFD software, which was utilized to generate a computational mesh for the various CFD solvers. The most significant advantage of utilizing unstructured tetrahedral meshes is the flexibility to handle complex geometries. Moreover, mesh generation time is significantly reduced compared with the use of structural hexahedral meshes. Unstructured tetrahedral meshes are suitable for solution-adaptive mesh refinement/coarsening techniques and particularly useful in capturing shocks. Finally, given the lack of overlapping mesh regions, fewer mesh nodes are required.

The solid boundary at the sabot and projectile is assumed to slip, and its wall is considered adiabatic. The pressure far-field condition was used for the inlet boundary. Characteristic analysis based on Riemann invariant was employed to determine the outlet boundary. The working fluid for this analysis was air with density calculated from the perfect gas assumption. The ambient pressure was 101325 Pa, and the gravitational acceleration was g = 9.8 m/s^2 with 300 K ambient temperature. Considering that sabot discard occurs within a relatively short distance from the muzzle, the incoming Mach number is assumed to be constant; its value is 4.0 with 0° angle of attack. Given that an implicit time-stepping algorithm is utilized, time step Δt is not limited by the stability of the flow solver and is selected based on the accuracy and stability of the dynamic meshing algorithm.

3. Results and discussion

3.1 Discard process

The pressure distribution contours in the symmetry plane (*xoy* plane) of the projectile/sabot during sabot discard are illustrated in Figs. 4-6. For the analysis of the complex aerodynamic interactions occurring between the projectile and the sabot, the discard process was divided into three phases based on their respective flow features.

Phase 1: Choked Flow

In this phase, choked flow is the dominant feature because the gaps among the sabots and projectile are not large enough to accommodate the incoming mass flow rate captured by the sabot front scoops. The interaction is characterized by a single detached normal shock (bow shock) formed upstream of the sabot petals and essentially a stagnant volume of air within an annular plenum chamber bounded by the front scoops of the sabot petals, as shown in Figs. 4(a) and (b). During this phase, the stagnant mass of air continues to increase because the incoming mass flow rate is greater than the outgoing one. The subsonic flow behind the bow shock is accelerated to supersonic as it passes through a series of expansion waves, similar to the acceleration of subsonic flow in a converging channel. A high-pressure region is created because of bow shock and remains until the disappearance of the choked flow (Figs. 4 and 5).

The pressure on the surface of sabots not only provides axial and radial forces for sabot discard but also produces moments that maintain the pitch motion of the sabot. Given the increase in distance among the petals and projectile, the incoming flow is no longer choked; the detached normal shock begins to move downstream, collides with the projectile, and leads to a sharp increase in pressure on the projectile surface (Figs. 4(c) and (d)). Then, the flow structure near the leading edge of the sabot begins to change from single detached normal shock to multiple bow shocks, with each shock emanating from an individual sabot petal. This action is the beginning of the second phase. Although the duration of the flow structure alteration is very short, it has a significant effect on sabot trajectory.

Phase 2: Oblique Shocks

In this phase, the flow structure is characterized by multiple bow and oblique shocks. The reflected shocks induced by the impinging of the oblique shocks on the projectile are shown in Fig. 5(a). The reflected shock moves downstream and changes its moving orientation during its interaction with the interior of sabots (Fig. 5(b)). Depending on the flow conditions and distance between the projectile and sabot, oblique shock may be reflected several times between the projectile and sabot and could result in pressure increase in the collision areas. Such a pressure fluctuation will modify the rotation and translation of the sabot and affect the flight stability of the projectile. As shown in Fig. 5, the sabot head lifts first; therefore, its radial distance to the projectile is larger than that of the tail.

With the increase in distance among the sabots and projectile, the pressure fluctuation induced by the reflected shock decreases and ultimately disappears along with the shock reflections. At this time, only the oblique shocks of sabots act on the tail of the projectile, and no reflected shock wave affects the sabot discard (Fig. 5(d)).

Phase 3: Free Flight of Sabots
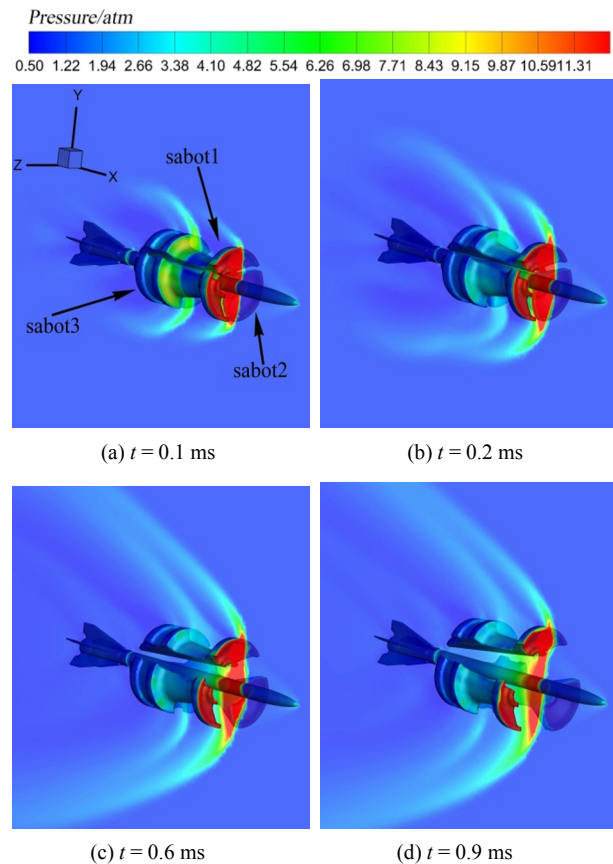
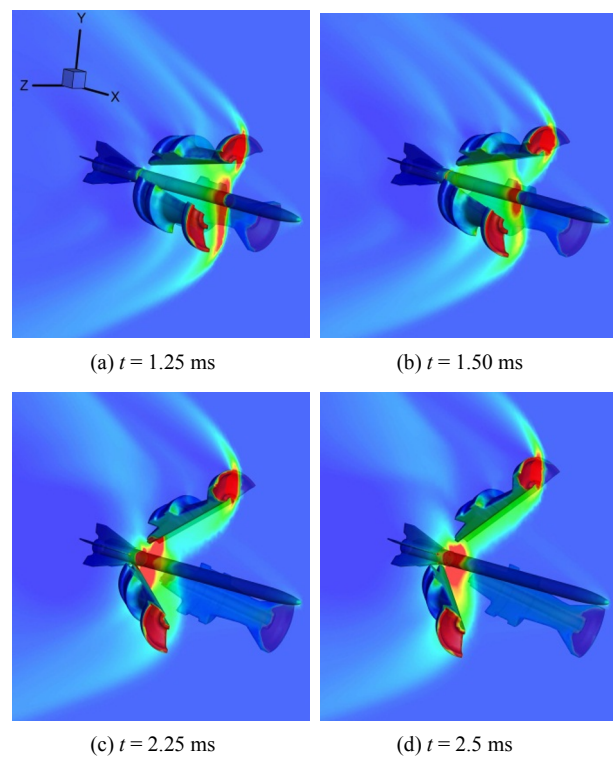As mentioned in Phase 2, when the area among the sabots

(a) $t = 0.1$ ms   (b) $t = 0.2$ ms

(c) $t = 0.6$ ms   (d) $t = 0.9$ ms

Fig. 4. Phase 1: choked flow.

(a) $t = 1.25$ ms   (b) $t = 1.50$ ms

(c) $t = 2.25$ ms   (d) $t = 2.5$ ms

Fig. 5. Phase 2: oblique shock.

(a) *t* = 3.00 ms   (b) *t* = 3.50 ms

(c) *t* = 4.50 ms   (d) *t* = 5.00 ms
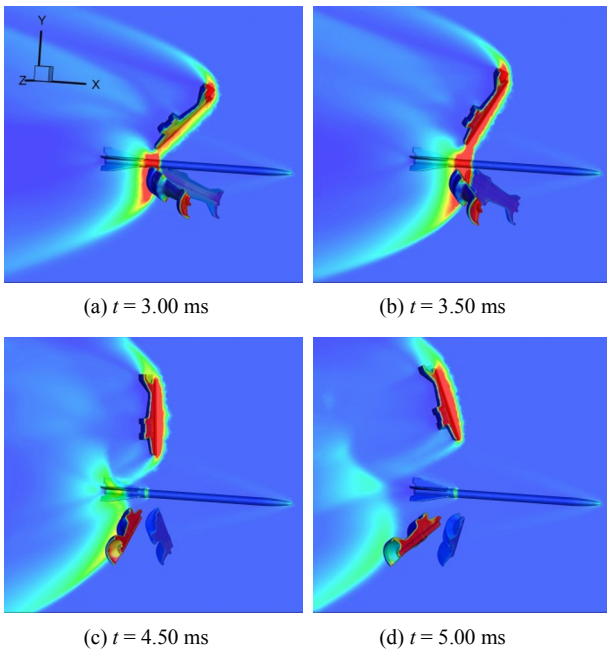
Fig. 6. Phase 3: free flight of sabots.

Fig. 7. Shock wave structure during discard [26].

(a) Sabot 1

(b) Sabot 2

(c) Sabot 3

Fig. 8. Discard processes of sabots.

and projectile is sufficiently large, the flow structure for each sabot is characterized by its bow shock (Fig. 6). The sabots rotate and translate independently under the action of aerodynamic forces. Owing to the sabot head lifting, the aerodynamic drag force of each sabot is very large and thus accelerates the movement of the sabot away from the projectile.

Meanwhile, the movement of the projectile is still under the effect of the bow shock of sabots (Figs. 6(a)-(c)). The bow shocks interact with the projectile tail and generate the pitch moment, which may reduce the stability of its flight. However, based on our simulation, bow shocks do not have much significance to the projectile at this stage because of their short action time.

Fig. 7 shows the experimental colored Schlieren picture from Ref. [26]. Our flow structures around the sabots and projectile agree well with those in the picture.
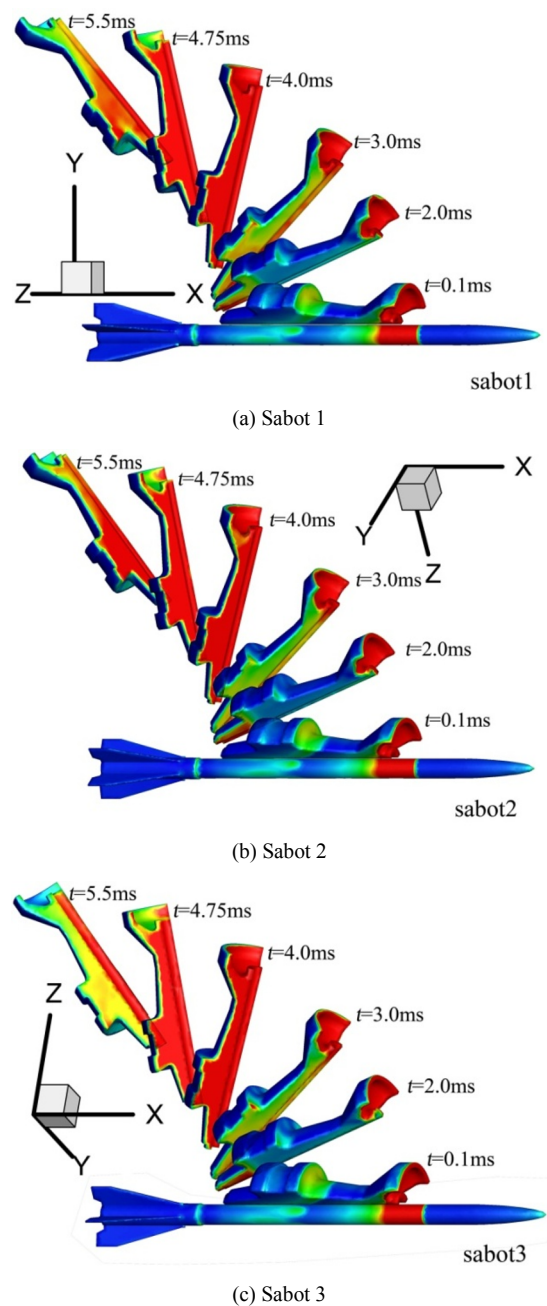
3.2 6DOF movement of sabots

Fig. 8 shows the positions and behavior of three sabot petals with respect to the projectile at six discrete times during the discard process. The discard process can be considered symmetric. The symmetric aerodynamic forces acting on the three sabot petals are supposed to cause such symmetric discard. Our results show that the separating movement of a sabot is dominated by its upturn along *x* direction; this result also agrees well with the experimental discard trajectory shown in Fig. 9 [27].
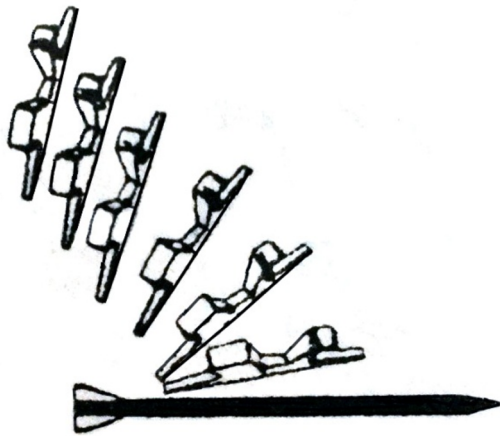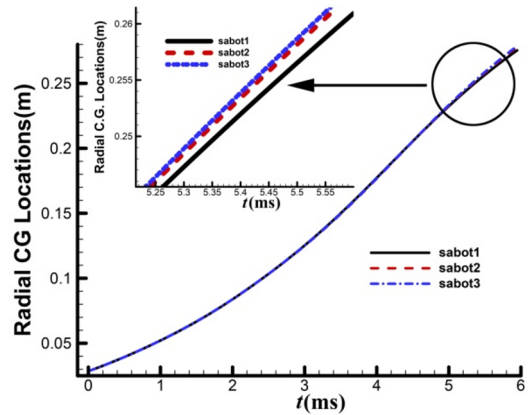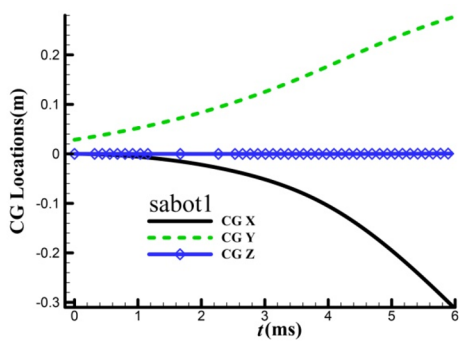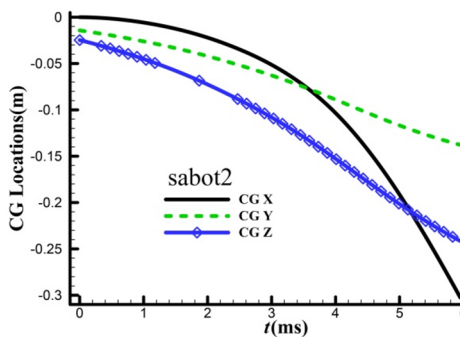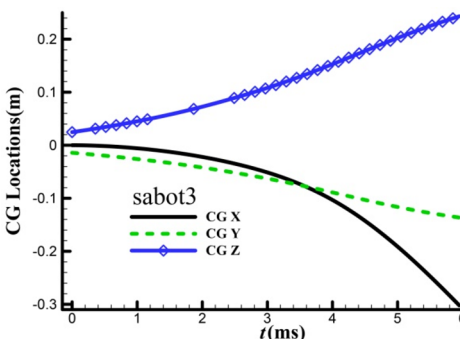
Fig. 9. Sabot separating trajectory [27].

Fig. 11. Radial center of gravity locations.

Fig. 10 shows the CG trajectories of three sabot petals in the inertial coordinate system. All three sabots move backward in the *x* direction because of the same aerodynamic drag. Along *y* direction, the locations of sabots 2 and 3 are almost similar and are symmetric to that of sabot 1. In *z* direction, sabot 1 is stationary, and the movement of sabot 2 is almost symmetric with that of sabot 3. As stated in Sec. 2.2, the movements of the three sabots are induced by their aerodynamic forces. The initial aerodynamic drag and lateral forces of these three sabots, which have the same shape and mass, are almost similar and lead to a nearly identical movement of sabots with respect to the projectile.

Fig. 11 presents the radial displacements of the three sabots with respect to the projectile. The radial displacements of the three sabots are similar before *t* = 5 ms. A discrepancy can be observed by zooming in Fig. 11 after *t* = 5 ms. This difference is caused by the various mesh sizes and the irregularity of tetrahedral mesh arrangement around the three sabots during the computation. The discard locations of each petal from lateral (a) and frontal (*x* direction, (b)) views are shown in Fig. 12.

Fig. 13 shows the CG velocities of three sabots in the inertial system. Their velocities in the *x* direction are almost similar. Along the *y* direction, the velocities of sabots 2 and 3 are similar and symmetric to that of sabot 1. Sabot 1 is stationary in the *z* direction, and the velocities of sabots 2 and 3 in the *z* direction are symmetrical.

The variations in Euler angles during discard were also calculated and are shown in Fig. 14. Fig. 15 presents their angular rates during discard. Pitch is the main moving feature of sabot 1, and almost no yaw and roll motion was observed. This result can be validated by the angular rates of sabot 1 (Fig. 15(a)). Sabot 2 (Fig. 14(b)) pitches down and yaws to the right during discard. In contrast, sabot 3 yaws to the opposite direction of sabot 2, but its pitch and angle rate distributions remain the same as those of sabot 2. All of the three sabots have small roll rates compared with their yaw and pitch rates.

Fig. 16 illustrates the force coefficient histories of the three sabots during discard. As shown in Fig. 16(a), the three sabots have almost the same drag coefficient because of their similar
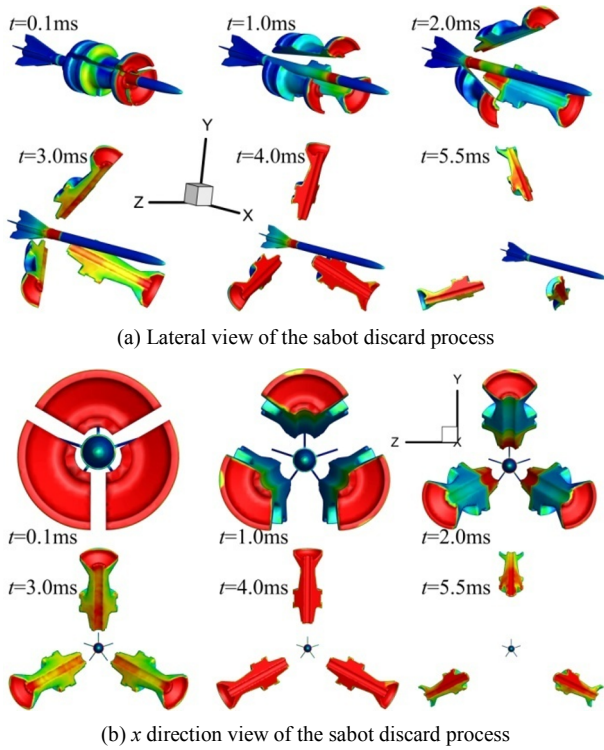

(a) Sabot 1

(b) Sabot 2

(c) Sabot 3

Fig. 10. Time evolution of the CG trajectory locations of three sabots.

(a) Lateral view of the sabot discard process

(b) *x* direction view of the sabot discard process

Fig. 12. Discard process from different angles of view.

(a) Sabot1

(b) Sabot2

(c) Sabot 3

Fig. 13. CG velocity of three sabots during discard.

movement in the *x* direction. Their fluctuations during discard (t ≤ 3.0 ms) are induced by the collision of reflected shock waves among the sabots and projectile.

In addition, the symmetric configuration of sabots 2 and 3 with respect to the *y* axis results in nearly similar lift coefficients during discard (Fig. 16(b)). Their lateral force coefficient distributions are symmetrical (Fig. 16(c)).

3.3 Aerodynamic coefficients of the projectile

During discard, the flight stability of the projectile is under the effect of sabots; therefore, the variations in its aerodynamic coefficients are critical. The time history curves of the projectile are shown in Fig. 17. The projectile is unaffected by the sabots after *t* ≥ 4.8 ms, which means that the sabots and projectile fly freely after this time. However, before this time, the aerodynamic coefficients of the projectile fluctuate under the actions of shock waves induced by the sabots.

Fig. 17(a) shows that the fluctuating amplitudes of drag (C_d) and lift (C_l) coefficients are larger compared with that of the lateral coefficient (C_z). This result is due to the symmetry of sabots 2 and 3; the impact of their shock waves on the projectile mainly causes the lift and lateral forces. However, the directions of their lateral forces are opposite and counteract each other, which reduces the total lateral force and causes it to fluctuate around the value of zero. Ultimately, it becomes zero because the projectile is in free flight.

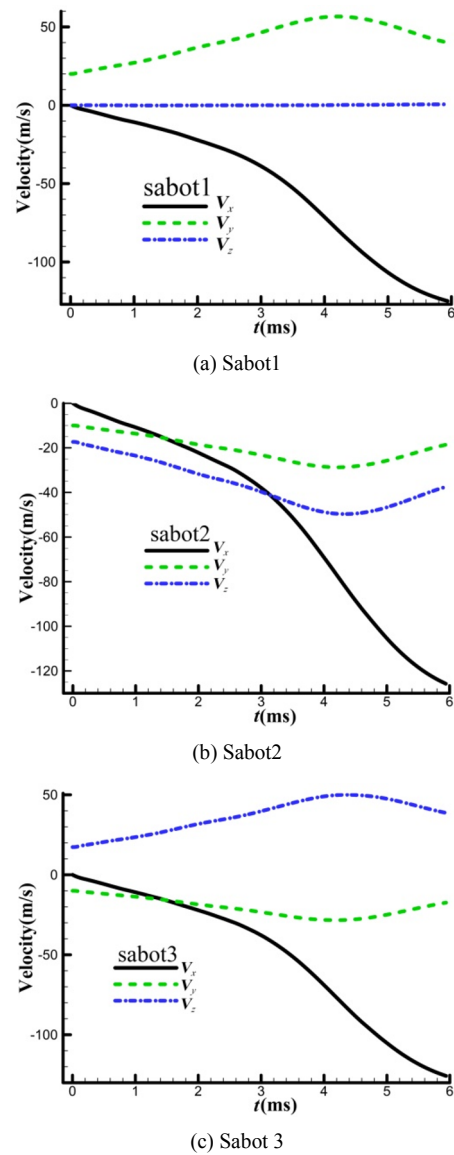The drag of the projectile is the largest under the actions of three oblique shock waves during phase 2. Its amplitude is the sum of the projection of three oblique shock waves along *x* direction. However, for the lift coefficient, the largest value appears at the end of the discard process. During this time, the shock waves impact the tail of the projectile almost perpendicularly, and the sum of lift generated by sabots 2 and 3 is far larger than that generated by sabot 1 (Figs. 6(b) and (c)). Therefore, a positive jump occurs.

This positive jump will induce a large fluctuation in the pitch moment (C_{Mz}, Fig. 17(b)) because the impact point at this stage is at the end of the projectile. The lift is positive; therefore, its induced pitch moment is negative. According to Fig. 17(b), the profile of the yaw moment (C_{My}) is similar to that of the lateral force coefficient (C_z). This result means that the yaw moment is induced mainly by lateral force. Additionally, no roll moment (C_{Mx}) is applied on the projectile during the discard process.
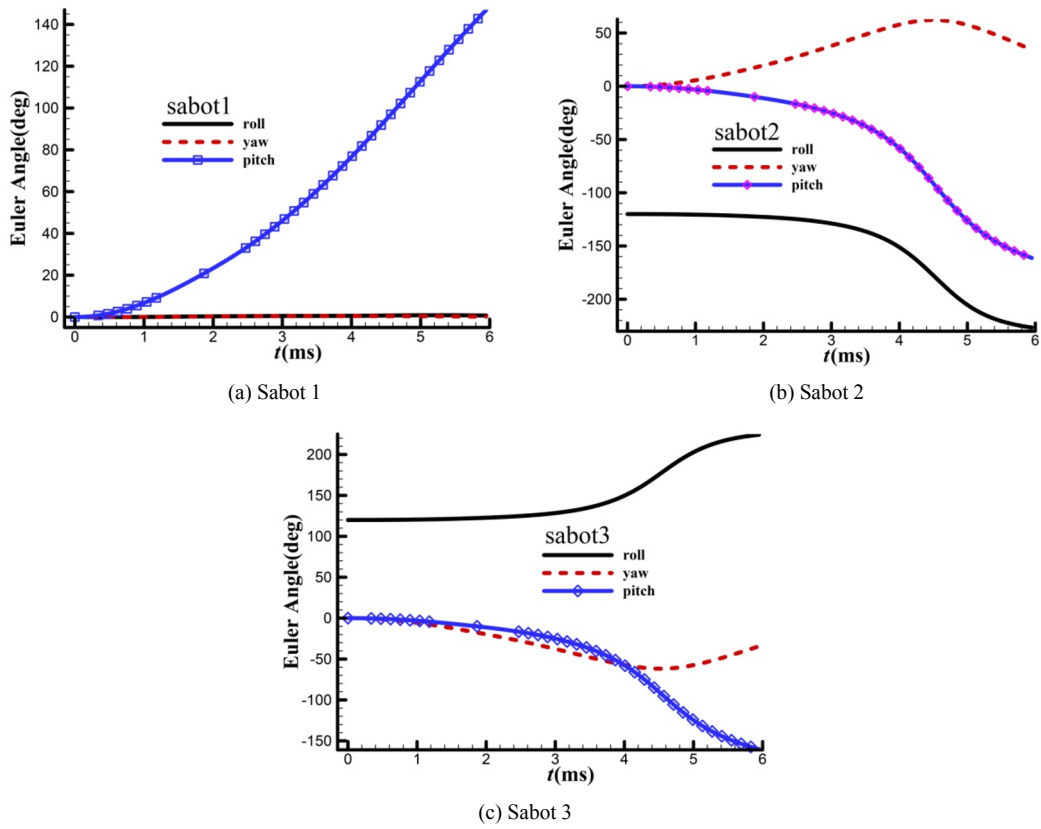
(a) Sabot 1

(b) Sabot 2

(c) Sabot 3

Fig. 14. Euler angles of the sabot discard process.

(a) Sabot 1

(b) Sabot 2

(c) Sabot 3
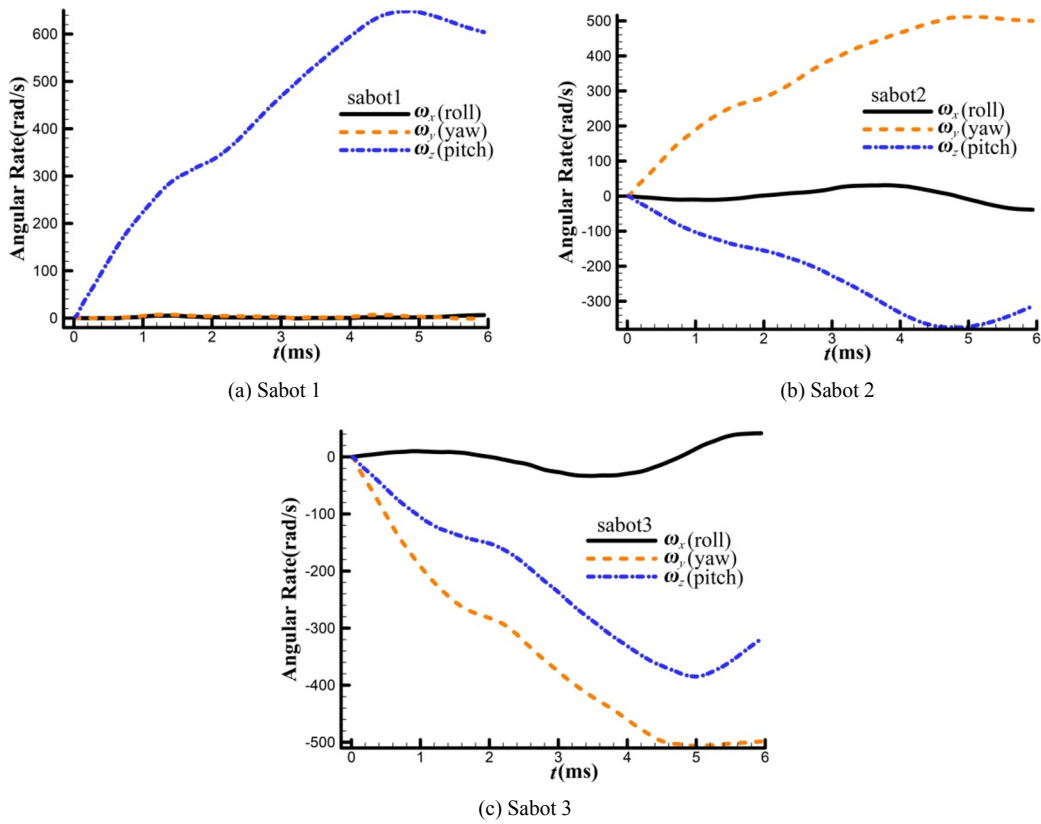
Fig. 15. Angular rates of three sabots during discard.

(a) C_d

(b) C_l

(c) C_z
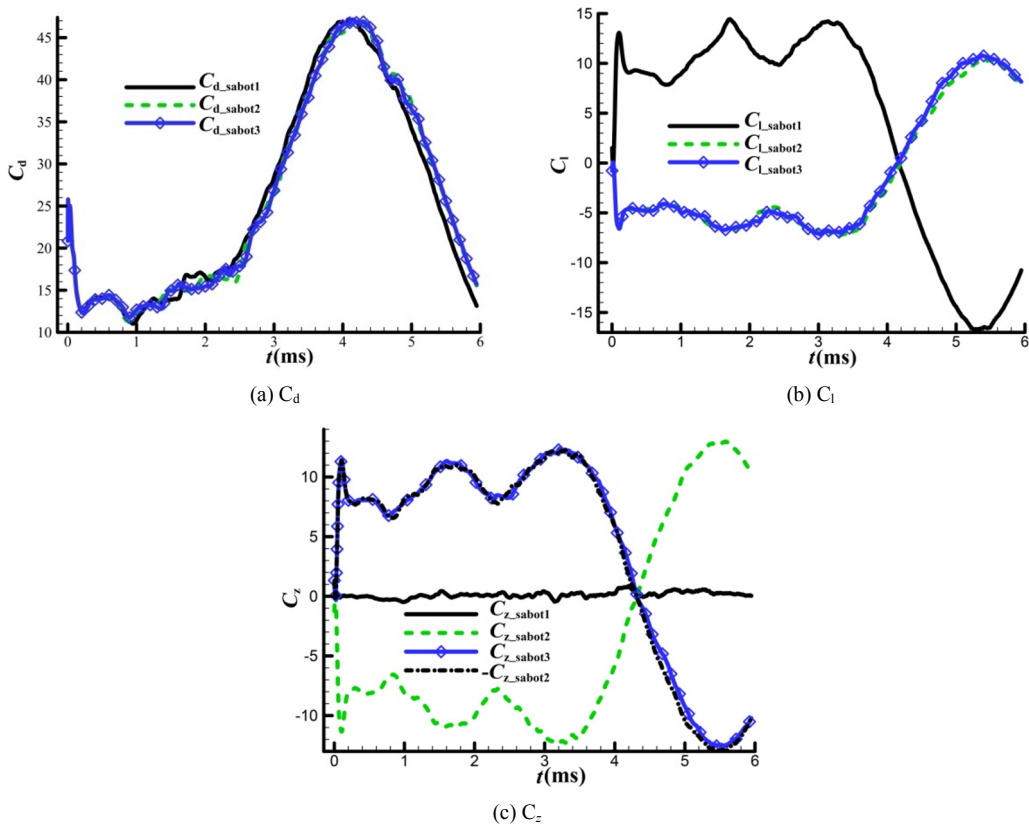
Fig. 16. Aerodynamic force coefficient histories of three sabots during discard.

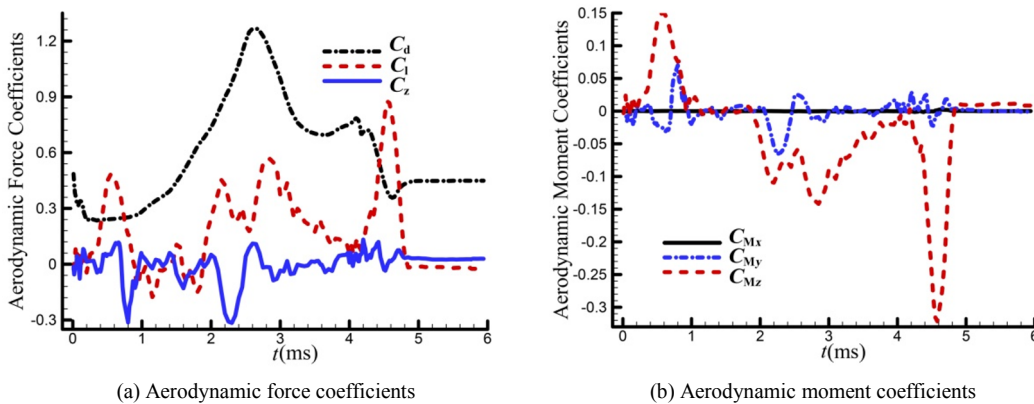(a) Aerodynamic force coefficients

(b) Aerodynamic moment coefficients

Fig. 17. Aerodynamic coefficient histories of the projectile during discard.

4. Conclusions

The dynamic discard process of sabots was simulated numerically by merging Euler and 6DOF rigid-body equations through UDF in FLUENT.

The numerical results agree well with those of the corresponding experimental investigations and illustrate the discard process in detail. Based on our investigations, three stages occur during discard. The first stage occurs at the beginning of discard, where high-speed flow accumulates at the front of the sabots because of the small gap between the sabot and projec-

tile; one bow shock of sabots appears. With the increase in the gap, the bow shock is divided into three parts, and each sabot has its own bow shock. Each bow shock impinges on the projectile and reflects back and forth; this occurs in phase 2. The last stage is the free flight of the sabots. Owing to the large gap between the sabot and projectile, the shock wave reflection is weak and ultimately has no effect on the sabot; however, the tail of the projectile is still under the action of oblique shocks of the sabots.

The flight characteristics of the sabots and projectile and their interactions were illustrated with the use of flight pa-

rameters calculated from 6DOF flight equations. The movement of a sabot is dominated by its upturn, and the movements of the three sabots are almost symmetrical with respect to the projectile. The effects of the sabots on the projectile during discard are mainly on the latter's drag and lift. The largest projectile drag value was obtained at phase 2. However, the largest lift and yaw moment appeared at the end of the discard process because of the collision of oblique shocks.

Acknowledgment

References

[1] H. Zhang, Z. Chen, X. Jiang and H. Li, Investigations on the exterior flow field and the efficiency of the muzzle brake, *Journal of Mechanical Science and Technology*, 27 (1) (2013) 95-101.

[2] R. Gopalapillai, H. D. Kim, T. Setoguchhi and S. Matsuo, On the near-field aerodynamics of a projectile launched from a ballistic range, *Journal of Mechanical Science and Technology*, 21 (7) (2007) 1129-1138.

[3] H. Rehman, S. H. Hwang, B. Fajar, H. Chung and H. Jeong, Analysis and attenuation of impulsive sound pressure in large caliber weapon during muzzle blast. *Journal of Mechanical Science and Technology*, 25 (10) (2011) 2601-2606.

[4] N. P. Bhange, A. Sen and A. K. Ghosh, Technique to improve precision of kinetic energy projectiles through motion Study, *AIAA Atmospheric Flight Mechanics Conference*, Chicago, Illinois, USA (2009) 1-33.

[5] E. M. Schmidt, Wind tunnel measurements of sabot discard aerodynamics, *Journal of Spacecraft and Rockets*, 18 (3) (1981) 235-240.

[6] E. M. Schmidt and D. D. Shear, Aerodynamic interference during sabot discard, *Journal of Spacecraft and Rockets*, 15 (3) 1978 162-167.

[7] E. M. Schmidt, Disturbances to the launch of fin-stabilized projectiles, *Journal of Spacecraft and Rockets*, 19 (1) (1982) 30-35.

[8] D. Siegelman, P. Crimi and E. Schmidt, Projectile/sabot discard aerodynamics, *6th Atmospheric Flight Mechanics Conference*, Danvers, Massachusetts, USA (1980) 280-286.

[9] J. N. Dick and D. S. Dolling, Pressure measurements on a Mach 5 sabot at different stages of the discard process, *27th Fluid Dynamics Conference*, New Orleans, LA, USA (1996) 1-15.

[10] J. N. Dick and D. S. Dolling, Pressure measurements on a Mach 5 sabot during discard, *Journal of Spacecraft and Rockets*, 35 (1) (1998) 23-29.

[11] Y. K. Lee, C. H. Tai, W. H. Hsi and M. F. Liu, High-resolution Navier-Stokes computations of a sabot separating form a gun-launched projectile with turbulence model, *14th International Symposium of Ballistics*, Quebec, Canada (1993) 519-527.

[12] P. Wu, W. Shang, R. Zhao and C. Chen, Three dimension numerical simulation for APFSDS sabots separating and discarding flow field, *ACTA Aerodynamica Sinica*, 23 (1) (2005) 1-4.

[13] L. E. Lijewski and N. E. Suhs, Time-accurate computational fluid dynamics approach to transonic store separation trajectory prediction, *Journal of Aircraft*, 31 (4) (1994) 886-891.

[14] N. C. Prewitt, D. M. Belk and W. Shyy, Parallel computing of overset grids for aerodynamic problems with moving objects, *Progress in Aerospace Sciences*, 36 (2) (2000) 117-172.

[15] M. K. Jung and O. J. Kwon, Development of 2-D flow solver on unstructured and adaptive Cartesian meshes, *Journal of Mechanical Science and Technology*, 26 (12) (2012) 3839-3997.

[16] D. O. Snyder, E. K. Koutsavdis and J. S. R. Anttonen, Transonic store separation using unstructured CFD with dynamic meshing, *33rd AIAA Fluid Dynamics Conference and Exhibit*, Orlando, Florida, USA (2003) 1-8.

[17] E. E. Panagiotopoulos and S. D. Kyparissis, CFD Transonic store separation trajectory predictions with comparison to wind tunnel investigations, *International Journal of Engineering*, 3 (6) (2010) 538-553.

[18] R. Cayzac, E. Carettean and T. A. De Roquefort, Intermediate ballistics unsteady sabot separation: first computations and validations, *19th International Symposium of Ballistics*, Interlaken, Switzerland (2001) 297-305.

[19] R. Cayzac, E. Carette, T. A. De Roquefort and P. Bidorini, Unsteady intermediate ballistics: 2D and 3D CFD modelling, application to sabot separation, *22th International Symposium of Ballistics*, Vancouver, Canada (2005) 398-404.

[20] R. Cayzac, E. Carette, T. A. De Roquefort, F. X. Renard, D. Roux, J. N. Party and P. Balbo, Computational fluid dynamics and experimental validations of the direct coupling between interior, Intermediate and Exterior Ballistics Using the Euler Equations, *Journal of Applied Mechanics*, 78 (6) (2011) 1-18.

[21] M. J. Nusca, Numerical simulation of sabot discard aerodynamics, *AIAA 9th Applied Aerodynamics Conference*, Baltimore, Maryland, USA (1991) 423-432.

[22] K. R. Heavey, J. Despirito and J. Sahu, *Computational fluid dynamics flow field solutions for a kinetic energy (KE) projectile with sabot*, ARL-MR-572, Army Research Laboratory, Aberdeen Proving Ground, MD, USA (2003).

[23] M. J. Guillot, R. Subramanian and W. G. Reinecke, A numerical and experimental investigation of sabot separation dynamics, *34th Aerospace Sciences Meeting and Exhibit*, Reno, NV, USA (1995) 1-8.

[24] S. E. Kim, S. R. Mathur, J. Y. Murthy and D. Choudhury, A Reynolds-Averaged Navier-Stokes solver using unstructured mesh-based finite-volume scheme, *36th Aerospace Sciences Meeting and Exhibit*, Reno, NV, USA (1998) 1-8.

[25] J. Qian, J. Han, Z. Huang and Z. Chen, Numerical simulation of two-dimension flow field for armor-piercing bullet of supersonic speed deshelling, *Journal of China Ordnance*, 32 (10) (2011) 30-32, 43.

[26] Bbs.tiexue.net: Armour Piercing [EB/OL], [2013-08-28], *http://bbs.tiexue.net/post_7005833_1.html*.

[27] Q. Yang and Z. Xu, *Dynamic of sabot discard*, fourth Ed.

National Defense Industry Press, Beijing, China (1996).

HUANG Zhen-gui received his MSc degree from the Key Laboratory of Transient Physics, Nanjing University of Science & Technology, in 2010. Mr. Huang is currently pursuing his Ph.D. in the same university. His research interests include computational fluid dynamics of supersonic flow, external ballistics theory, and its application.

CHEN Zhi-hua received two Ph.D. degrees; one is from the New Jersey Institute of Technology, USA in 2001, and the other is from Nanjing University of Science & Technology, China, in 1997. Dr. Chen is currently a professor at the Key Laboratory of Transient Physics at Nanjing University of Science & Technology, Nanjing, China. His research interests include supersonic and hypersonic flow, detonation, and flow control.